

# Mesoscale tissue properties and electric fields in brain stimulation – bridging the macroscopic and microscopic scales

Boshuo Wang<sup>1</sup>, Torge Worbs<sup>2,3</sup>, Minhaj A. Hussain<sup>4</sup>, Aman S. Aberra<sup>5,6</sup>, Axel Thielscher<sup>2,3</sup>, Warren M. Grill<sup>4,7,8,9</sup>, and Angel V. Peterchev<sup>1,4,7,8,\*</sup>

<sup>1</sup> Department of Psychiatry and Behavioral Sciences, Duke University, Durham, NC, USA

<sup>2</sup> Section for Magnetic Resonance, DTU Health Tech, Technical University of Denmark, Kgs Lyngby, Denmark

<sup>3</sup> Danish Research Centre for Magnetic Resonance, Department of Radiology and Nuclear Medicine, Copenhagen University Hospital Amager and Hvidovre, Copenhagen, Denmark

<sup>4</sup> Department of Biomedical Engineering, School of Engineering, Duke University, Durham, NC, USA

<sup>5</sup> Department of Biological Sciences, Dartmouth College, Hanover, NH, USA

<sup>6</sup> Department of Molecular and Systems Biology, Dartmouth College, Hanover, NH, USA

<sup>7</sup> Department of Electrical and Computer Engineering, School of Engineering, Duke University, Durham, NC, USA

<sup>8</sup> Department of Neurosurgery, School of Medicine, Duke University, Durham, NC, USA

<sup>9</sup> Department of Neurobiology, School of Medicine, Duke University, Durham, NC, USA

\* Corresponding author

Emails: [boshuo.wang@duke.edu](mailto:boshuo.wang@duke.edu), [torwo@dtu.dk](mailto:torwo@dtu.dk), [minhaj.hussain@duke.edu](mailto:minhaj.hussain@duke.edu), [aman.s.aberra@dartmouth.edu](mailto:aman.s.aberra@dartmouth.edu), [axthi@dtu.dk](mailto:axthi@dtu.dk), [warren.grill@duke.edu](mailto:warren.grill@duke.edu), and [angel.peterchev@duke.edu](mailto:angel.peterchev@duke.edu)

## Abstract

Accurate simulations of electric fields (E-fields) in brain stimulation depend on tissue conductivity representations that link macroscopic assumptions with underlying microscopic tissue structure. Mesoscale conductivity variations can produce meaningful changes in E-fields and neural activation thresholds but remain largely absent from standard macroscopic models. Recent microscopic models have suggested substantial local E-field perturbations and could, in principle, inform mesoscale conductivity. However, the quantitative validity of microscopic models is limited by fixation-related tissue distortion and incomplete reconstruction of extracellular space. We outline approaches that bridge macro- and microscales to derive consistent mesoscale conductivity distributions, providing a foundation for accurate multiscale models of E-fields and neural activation in brain stimulation.

Accurate modeling of the electric fields (E-fields) generated by brain stimulation modalities is crucial for estimating the stimulation dose [1], understanding the neural responses [2], and improving performance via computational optimization [3]. Conventional E-field simulations assume homogeneity of tissue electrical properties on the macroscopic scale that represents an average of the microscopic cellular composition [4]. Unlike previous microscopic E-field simulations restricted to only a few simplified cells [5], the latest models captured much larger tissue volumes with morphologically-realistic cells reconstructed from electron microscopy [6]. The models enabled the evaluation of the effects of microscopic E-field perturbations on neural activation thresholds in response to, for example, transcranial magnetic stimulation [6–9], and sparked constructive debates about the uses and limits of microscopic models [4,8–10]. Here, we summarize and extend these discussions and outline a path toward coherent multiscale modeling frameworks of E-fields and neural activation for brain stimulation that span the macro-, meso-, and microscales<sup>1</sup> [4].

Finite- and boundary-element head models typically assign constant conductivity to each tissue volume, constrained by computational cost and the lack of spatially-distributed measurements. Mesoscopic inhomogeneity, such as layer- or depth-dependent conductivity in the gray matter [11,12] or retina [13–15], is available but only rarely modeled [16,17]. An important exception is white matter anisotropy modeled on diffusion tensor imaging data: the conductivity tensor varies on the mesoscale, although its magnitude is usually derived from a fixed equivalent isotropic conductivity value [18]. Major challenges also remain regarding partial volume effects at tissue boundaries due to the limited spatial resolution and lack of consensus on diffusion-conductivity mappings [18,19]. Such mesoscopic conductivity variations in macroscopic models are expected to affect the E-field [20] and hence activation thresholds [17], as the E-field can vary over distances comparable or larger than neuronal length constants. In contrast, microscopic E-field variations are spatially filtered by the neural membranes and average out on the mesoscale<sup>2</sup> to mean values [10] that depend on the underlying cellular density and extracellular volume fraction [9]. The mesoscopic E-field variations led to changes in activation thresholds of up to 30% in

---

<sup>1</sup> Microscale corresponds to sizes of cellular and sub-cellular structures in the range of nanometers to tens of micrometers. Macroscale, in the broader sense, refers to any tissue volumes larger than microscale for which the underlying cellular composition can be (locally) homogenized. Depending on the model size and stimulation modality, macroscale can be considered on the order of several millimeters in size or larger, e.g., full head model for transcranial electromagnetic stimulation based on millimeter-resolution imaging data. In this context, the two orders-of-magnitude in between the microscale and macroscale are considered the mesoscale. In other cases, e.g., deep brain stimulation or vagus nerve stimulation with implanted electrodes, macroscale corresponds to sizes of the electrode and subcortical nuclei or fascicle, which is similar to mesoscale for a full head model, and there is no clear distinction between macro- and mesoscales.

<sup>2</sup> Due to the fact that macroscopic E-field models almost always use homogenous conductivities despite being capable of simulating inhomogeneity, the term “macroscopic” could be confused with “homogenous” [9]. Mesoscale conductivity also represents averages of microscopic cellular composition, in contrast to microscopic models that explicitly represent underlying cell structures.

specific neuron models [9]. Accounting for the microscopic structure [4], a model has captured variations in the gray matter effective conductivity not only across layers but potentially also over short distances along the cortex within the same layer [9]. However, the assumption of such strong intra-layer conductivity contrast needs to be experimentally validated, due to the modeling method simplifying the extracellular space as discussed below. Given the importance of mesoscale conductivity variations for E-field and neural simulations, we outline approaches bridging macro- and microscale data to derive mesoscale conductivity<sup>3</sup> distributions.

Approaching from the macroscale, higher resolution imaging can generate tissue models that capture mesoscale features, such as meninges, large vasculature, cortical layers, nuclei, or other variation in tissue properties within brain regions, and even microscopic structures within a region of interest [22]. However, electrical properties are mostly measured on macroscales and distributions on the mesoscale are not available for most tissue types. Conventional metal microelectrodes and electrode arrays for impedance measurements average conductivity over relatively large volumes [14], whereas fine-tipped ( $\sim 1 \mu\text{m}$ ) glass micropipettes can resolve fine conductivity changes (Fig. 1A). Unlike sharp tissue conductivity boundaries in models, actual transitions of tissue composition (e.g., from gray matter to white matter) are smoother [16,23]. Therefore, measurements must distinguish true conductivity gradients from artifacts introduced by the electrodes and tissue preparation (Fig. 1A). Applying macroscale electric impedance tomography principles to multi-electrode arrays [24,25] could measure mesoscale conductivity distributions within brain tissue samples *in vitro*. Such systems require dense electrode coverage and careful calibration. Alternatively, multi-contact electrodes [12,20] can be used to measure spatial electric field profiles during local microsimulation [26] or transcranial stimulation [20], enabling conclusions about mesoscale conductivities and their spatial variations.

Approaching from the microscale, tissue conductivity can be modeled using simplified geometries [27–29] and extracellular volume fraction data [30] (see Appendix) or realistic tissue structure from electron microscopy [4,9,17]. However, most electron microscopy methods, including those used in recent large-scale connectomics projects [23,31], rely on chemical fixation, which causes tissue shrinkage due to dehydration and distortions of cellular structure [32–34]. Chemical fixation results in an almost complete absence of the 40–80 nm wide extracellular gaps between cell membranes [35], leading to direct contacts between neighboring membranes [32] and underestimation of the extracellular volume fraction (Fig. 1B). This issue is mitigated in tissues processed with cryofixation, but to what extent the reconstructed cells are free from distortion is unknown. In a recent microscopic E-field model [6,7], the

---

<sup>3</sup> Here we focus on low-frequency, quasistatic conductivities relevant for transcranial electrical and magnetic stimulation [21]; frequency-dependent and non-ohmic aspects of tissue impedance are important but largely orthogonal to the mesoscale spatial questions highlighted here.

tissue had a volume fraction of “extracellular space” around 70%, much larger than the 15%–30% range obtained from *in vivo* diffusion studies [30]. This discrepancy appears to arise because the model’s “extracellular space” subsumed intracellular regions of omitted cell structures (e.g., neurites belonging to somata outside the sample and very small neuroglia cells; Fig. 1C). Thus, though these microscopic models provide valuable insight into E-field distortions around complex morphologies, their current treatment of extracellular space limits their use for quantitative conductivity estimation. Super-resolution optical microscopy enables nanoscale reconstruction of brain tissue in living samples while avoiding fixation- or freezing-induced artifacts [36], but these methods are limited to shallow depths due to light scattering and are still not viable *in vivo*. With enhancements of these techniques, structural imaging could be combined with physiological measurements in the same preparation to build microscale reconstructions that accurately capture the extracellular space, identify sufficient levels of biophysical detail for predictive models, and validate statistical averaging across neurons within a tissue volume and across subjects.

Despite the numerous challenges of both macroscale and microscale approaches, these methods complement and validate each other and should converge on consistent mesoscale distribution of tissue conductivity. Overcoming technical limitations via collaboration across different fields, including biophysics and physiology, electrode microfabrication, high resolution imaging, and computational modeling, the quality of E-field models and neural simulations for brain stimulation can be improved by accurate representation of tissue conductivity on the mesoscale.

#### **Declaration of Competing Interest**

B. Wang, T. Worbs, M. A. Hussain, A. S. Aberra, A. Thielscher, and W. M. Grill declare no relevant conflict of interest. Related to TMS technology, A. V. Peterchev has received patent royalties and consulting fees from Rogue Research; equity options, scientific advisory board membership, and consulting fees from Ampa Health; equity options, consulting fees, and travel support from Magnetic Tides; consulting fees from Soterix Medical; equipment loans from MagVenture; and research funding from Motif.

#### **Acknowledgments**

This work was supported by the National Institute of Mental Health of the US National Institutes of Health under grant No. R01MH128422 and U01NS126052. A. Thielscher was supported by the Lundbeck Foundation (grant R313-2019-622). The content is solely the responsibility of the authors and does not necessarily represent the official views of the funding agency.

#### **CRedit authorship contribution statement**

B. Wang: Conceptualization, Investigation, Formal analysis, Visualization, Writing—original draft, Writing—review & editing. T. Worbs: Investigation, Formal analysis, Visualization, Writing—review & editing. M. A. Hussain: Investigation, Writing—review & editing. A. S. Aberra: Investigation, Writing—review & editing. A. Thielscher: Conceptualization, Funding acquisition, Writing—review & editing. W. M. Grill: Conceptualization, Funding acquisition, Writing—review & editing. A. V. Peterchev: Conceptualization, Funding acquisition, Writing—review & editing.

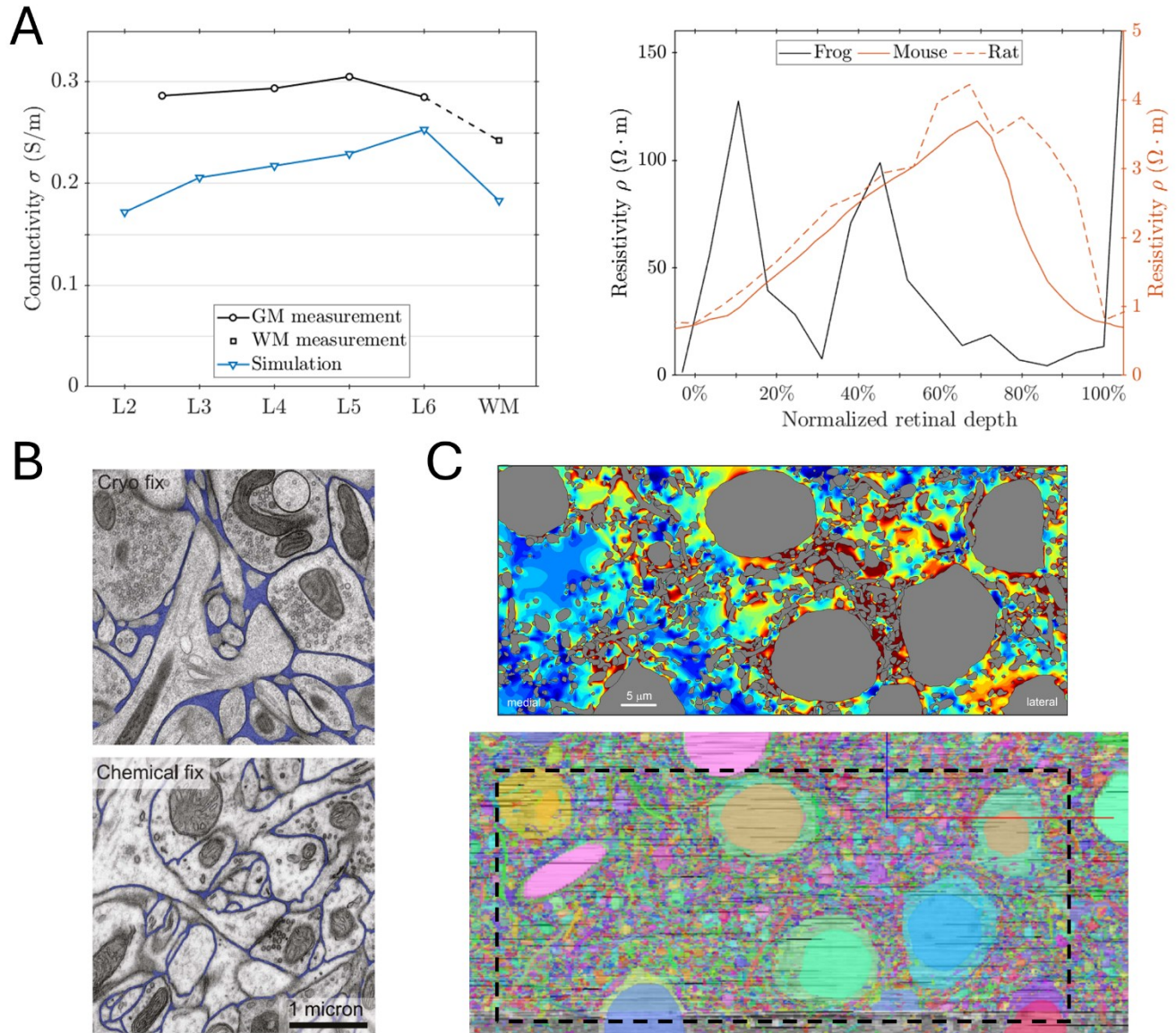


**Figure 1** Comparing mesoscopic conductivity profiles of neural tissue obtained with different methods. Left: Equivalent isotropic conductivity of gray matter measured in the rat cortex (black circles) using electrode arrays with 15 and 30  $\mu m$  diameter electrodes [12], with layers 2 and 3 considered as a single layer, and equivalent isotropic conductivity of white matter measured in the cat internal capsule (black square) using a wire probe [37]. The isotropic conductivity estimated using a computational model (blue triangles) [29] based on extracellular volume fraction in rat cortex and subcortical white matter obtained from ion diffusion measurements with ion-sensitive glass microelectrodes of  $\sim 1\text{-}\mu m$  diameter [30] (see Appendix for detailed modeling methods and results). Right: Depth-dependent resistivity of the retina, with normalized depth of 0% indicating the retinal ganglion cell side and 100% indicating the photoreceptor side. Measurements using ion-selective micropipettes with sub-micrometer diameter in a frog eyecup (right axis, black line) show distinct variation with depth and much higher conductivity values due to the intact retinal pigment epithelium [13]. Measurements using microelectrodes in isolated rodent retina without the highly-resistive retinal pigment epithelium show lower resistivity and smooth profiles

that average the conductivity of distinct layers and surrounding saline due to spatial averaging of the electrodes and tissue distortion and disruption during electrode insertion [14] (right axis, orange solid line: bipolar microelectrode with a conic inner pole of 25  $\mu\text{m}$  diameter and 25  $\mu\text{m}$  height and concentric outer pole [14]; orange dashed line: microelectrode array with 40  $\mu\text{m}$   $\times$  25  $\mu\text{m}$  rectangular electrodes spaced 10  $\mu\text{m}$  apart [15]). **B.** Electron microscopy images of tissue processed with cryofixation (top) and chemical fixation (bottom) show significant difference in extracellular space (pseudo-colored in blue) among other fixation-induced changes [32]. **C.** Top: Microscopic E-field simulation [6,7] showing large extracellular space (color map showing E-field) with  $\sim 70\%$  volume fraction and small intracellular space (gray) of  $\sim 30\%$  volume fraction. Bottom: Electron microscopy of the MICrONS dataset of mouse visual cortex [31] on which the microscopic E-field simulations were based showing the same frame (dashed outline). The micrograph reveals dense cellular and subcellular composition (filled with random colors) with almost no extracellular space, indicating that the “extracellular space” in the simulation is dominated by the intracellular space of excluded cells.

Panel B adapted from Ultrastructural Analysis of Adult Mouse Neocortex Comparing Aldehyde Perfusion with Cryo Fixation, by N. Korogod et al., 2015, eLife, vol. 4, p. e05793. Copyright 2015 by The Authors. Adapted under the Creative Commons Attribution License (CC BY 4.0). Top part of panel C adapted from Statistical Method Accounts for Microscopic Electric Field Distortions Around Neurons When Simulating Activation Thresholds, by K. Weise et al., 2025, Brain Stimulation, vol. 18, no.2, p. 281. Copyright 2025 by The Authors. Adapted under the Creative Commons Attribution License (CC BY-NC 4.0). Bottom part of panel C obtained from [www.microns-explorer.org](http://www.microns-explorer.org).

## Appendix

To obtain mesoscopic conductivity values from microscopic cellular structures, we examine how the conductivity of neural tissue varies as a function of cell density and thus volume fraction using computational models. We first review theoretical formulas from the literature, which are compared against the simulated results. As layer-specific cellular volume fractions are not directly available, complementary volume fractions of extracellular space from diffusion experiments were used.

### **Theoretical formulas for conductivity–cell volume fraction relationship**

Previous studies [38–41] modeled the relationship between effective conductivity  $\sigma$  and volume fraction of cells  $f$  (Table A1). Most methods assumed a low volume fraction for cell suspension, with the conductivity of the extracellular fluid as  $\sigma_0$  and homogenous cell conductivity, which can be set to zero for simplicity.

### **Layer-specific volume fraction of extracellular space and cells in brain**

We used the volume fraction of extracellular space,  $\alpha$ , obtained by Lehmenkühler et al. with *in vivo* diffusion methods in somatosensory cortex and subcortical white matter of adult (90 to 120 days old) rats (Table A2) [30]. In summary, tetramethylammonium concentration was measured with ion-selective microelectrodes positioned 130–200  $\mu\text{m}$  from an iontophoretic source and the concentration versus time curves were fitted to diffusion equations assuming spherical symmetry to extract parameters including  $\alpha$ , tortuosity, and cellular uptake. The volume fractions of cells were given as  $f = 1 - \alpha$ .

**Table A1** Theoretical conductivity–cell volume fraction relationship

Formula	Notes	Sources
$\frac{\sigma}{\sigma_0} = \frac{1-f}{1+f/2} = 1 - \frac{3f}{2+f}$	Dilute cell suspension, simplified for non-conducting spheres	[38,41]
$\frac{\sigma}{\sigma_0} = 1 - \frac{3f}{2+f - 0.394 \cdot f^{\frac{10}{3}}}$	Spherical particles arranged in a simple cubic lattice, simplified for non-conducting spheres.	[39,41]
$\frac{\sigma}{\sigma_0} = 1 - \frac{3f}{2+f - \frac{0.986 \cdot f^{\frac{10}{3}}}{1 - 0.307 \cdot f^{\frac{7}{3}}}}$	Spherical particles arranged in a simple cubic lattice, simplified for non-conducting spheres.	[42]
$(1-f)^{\frac{5}{3}} \leq \frac{\sigma}{\sigma_0} \leq (1-f)^{\frac{3}{2}}$	Elongated homogeneously distributed randomly orientated non-conducting spheroids	[40]
$\frac{\sigma}{\sigma_0} = \begin{cases} (1-f)^1 \\ (1-f)^2 \end{cases}$	Parallel fibers, longitudinal Parallel fibers, transverse	[40]

**Table A2** Volume fraction of extracellular space and cells [30]

Layer	Volume fraction of extracellular space, $\alpha$	Volume fraction of cells, $f$
L1	Not available	Not available
L2	17%	83%
L3	20%	80%
L4	21%	79%
L5	22%	78%
L6	24%	76%
White matter	18%	82%

***Tissue models and simulation setup [29]***

We built cubic blocks of simplified microscopic cellular representation of several tissue types using finite element models in COMSOL (version 6.2, COMSOL, Inc.). Conductivities of cell membranes and the intra- and extra-cellular spaces were assigned according to literature (Table A3). The cell volume fraction varied in steps of 5% from 5% to 95% or within the maximum allowed by the specific tissue model (Table A4), and different cell shapes and orientations of the tissue structure were modeled to test their influence on the conductivity. The electric potential and electric field (E-field) distributions were simulated in the tissue for 1  $\mu$ A current applied on one side of the sample with a floating potential boundary condition. The opposite side was grounded, and the remaining four sides were insulated. The resulting electrode floating potential was used to calculate the total resistance of the tissue block. The effective tissue conductivity for a given tissue type was then calculated and averaged for various cell shapes and rotational orientations of the tissue structure. The conductivities of different cortical layers (layers 2 to 6) were interpolated based on experimental volume fraction in the range of 70% to 90%. Data analysis and additional visualization were performed in MATLAB (version 2024b, The MathWorks, Inc.).

***Parallel axons***

Cylinders and hexagonal prisms [43,44] placed in hexagonal grids were used to represent parallel axons (Fig. A1 and Table A4). The length of the unit cell (parallelogram) was 10  $\mu$ m. Circular cross-section allows cell volume fraction up to 90.7%, whereas hexagonal prisms allow denser packing theoretically achieving 100% volume fraction. Given the longitudinal symmetry along the axons' axes, a 2D model was built with the axial direction not explicitly represented. The tissue blocks were 180  $\times$  180  $\times$  180  $\mu$ m<sup>3</sup> in size and the orientation of the grid pattern was rotated up to 30° in steps of 5°.

### Cell bodies

Spheres [41] and truncated octagons [45] placed in body-centered cubic lattice with a unit cell of  $10\ \mu\text{m}$  side length were used to represent tight packing of cells (Fig. A2 and Table A4), with the former being limited to a volume fraction of 68%. The 3D tissue block was  $60 \times 60 \times 60\ \mu\text{m}^3$  in size and three tissue orientations, corresponding to Miller indices of 100, 110, and 111 of the lattices, were used.

### Interleaved neurites (neuropil)

3D-crosses with circular and square cross-section placed in body-centered cubic lattice were used to represent densely interleaved neural branches in the neuropil (Fig. A3 and Table A4), with the 3D model setup similar to that of the cell bodies.

**Table A3** Model parameters

Parameter	Symbol	Value	Unit
Extra- and intracellular conductivity	$\sigma_0$	1	$\text{S}\cdot\text{m}^{-1}$
Membrane conductivity	$\sigma_m$	$10^{-8}$	$\text{S}\cdot\text{m}^{-1}$
Membrane thickness	$t_m$	10	nm
Specific membrane resistance	$R_m$	1	$\Omega\cdot\text{m}^2$
Unit cell side length	$d$	10	$\mu\text{m}$

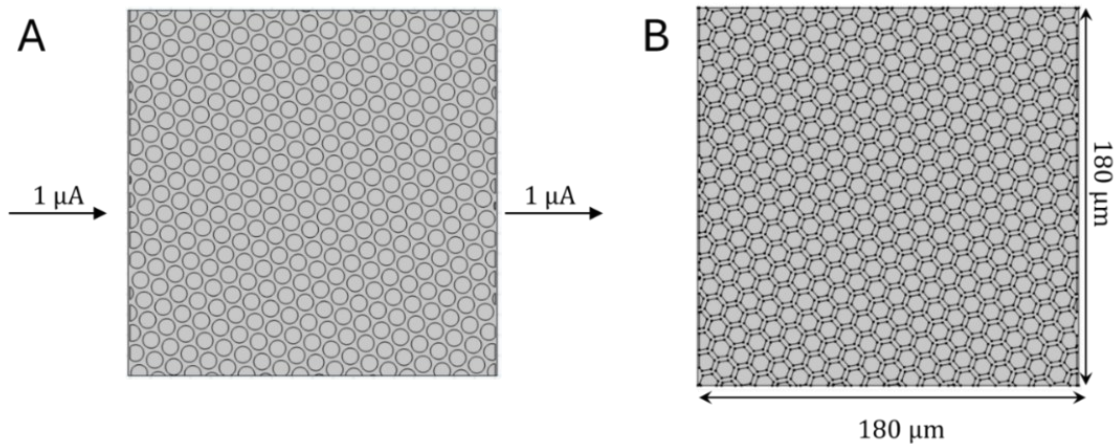


**Figure A1** Axons transverse to the current direction modeled as hexagonal grids of cylinders (**A**) and hexagon prisms (**B**). The 2D model had an implicit depth of  $180\ \mu\text{m}$ . Both axon grids had a cell volume fraction of 60% and rotation of  $20^\circ$ .  $0.5\ \mu\text{m}$ -wide gaps were added on both the left and right sides to avoid direct contact between the electrodes and cell membrane.

**Table A4** Models and parameters for representing different neural tissue types

Dimension and model representation	Lattice with unit cell of side length $d$ and orientations explored	Shape of cells or their cross sections, Side length $\hat{a}$ or radius $\hat{r}$ (normalized to $d$ )	Volume fraction $f$ and limits (if less than 100%)	Inverse relationship of volume fraction and neuron size	
2D, parallel axon fibers, transverse	Hexagon grid, $0^\circ$ to $30^\circ$ , in steps of $5^\circ$	Hexagon	$\hat{a} \leq \frac{1}{\sqrt{3}}$	$f = 3\hat{a}^2$	$\hat{a} = \sqrt{\frac{f}{3}}$
		Circle	$\hat{r} \leq \frac{1}{2}$	$f = \frac{2\pi}{\sqrt{3}}\hat{r}^2 \leq 90.7\%$	$\hat{r} = \sqrt[4]{\frac{f}{2\pi}}$
3D, cell bodies	Body-centered cubic lattice, Miller-indices 100, 110, 111	Truncated octahedron	$\hat{a} \leq \frac{1}{2\sqrt{2}}$	$f = (2\sqrt{2}\hat{a})^3$	$\hat{a} = \frac{\sqrt{2}\sqrt[3]{f}}{4}$
		Sphere	$\hat{r} \leq \frac{\sqrt{3}}{4}$	$f = \frac{8\pi}{3}\hat{r}^3 \leq 68.0\%$	$\hat{r} = \sqrt[3]{\frac{3f}{8\pi}}$
3D, dense interleaved neurites	Miller-indices 100, 110, 111	3D cross with length $d$ and square cross section	$\hat{a} \leq \frac{1}{2}$	$f = 2(3 - 2\hat{a}) \cdot \hat{a}^2$	$\hat{a} = \cos\left[\frac{\arccos(1-f) - 2\pi}{3}\right] + \frac{1}{2}$
		3D cross with length $d$ and circular cross section	$\hat{r} \leq \frac{1}{4}$	$f = (6\pi - 16\sqrt{2}\hat{r}) \cdot \hat{r}^2 \leq 82.5\%$	$\hat{r} = \frac{\pi}{4\sqrt{2}}\left\{\cos\left[\frac{1}{3}\arccos\left(1 - \frac{32f}{\pi^3}\right) - \frac{2\pi}{3}\right] + \frac{1}{2}\right\}$

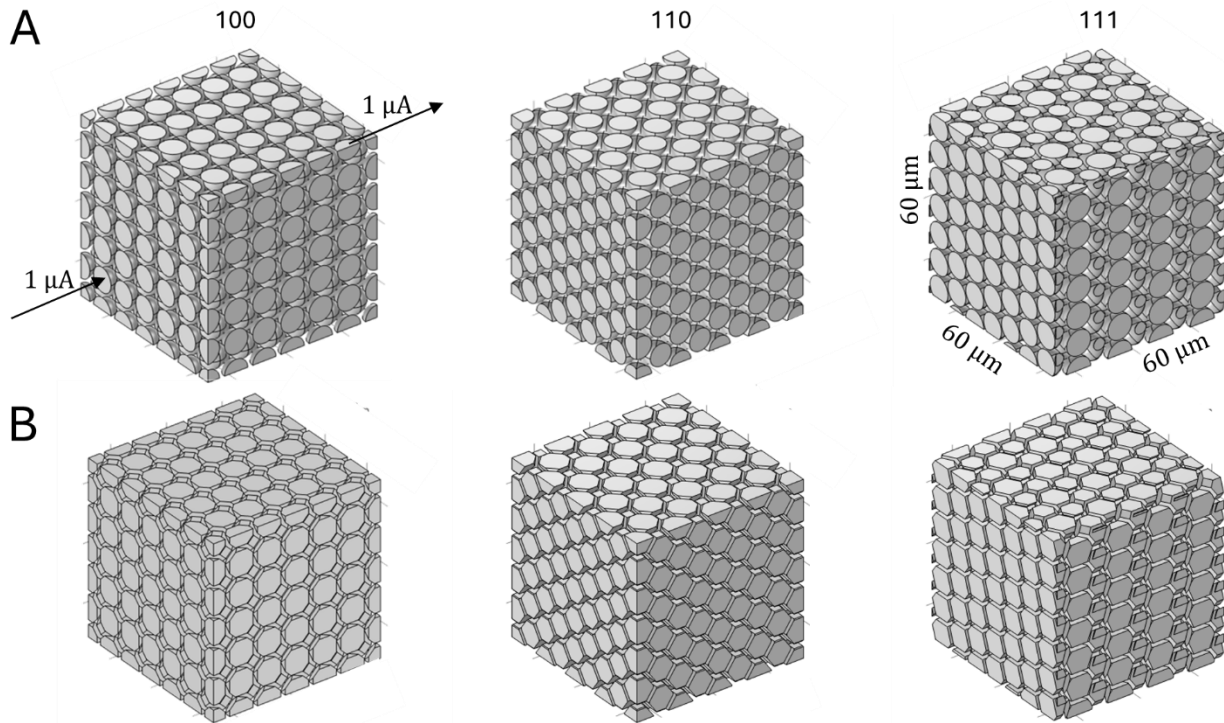


**Figure A2** Cells modeled as body-centered cubic lattices of spheres (**A**) and truncated octagons (**B**). The current was aligned with the 100 (left), 110 (middle), and 111 (right) orientations of lattices, which all had a cell volume fraction of 60%. The outer boundaries of the models are not shown. 0.5  $\mu\text{m}$ -wide gaps were added on both the left and right sides to avoid direct contact between the electrodes and cell membrane.

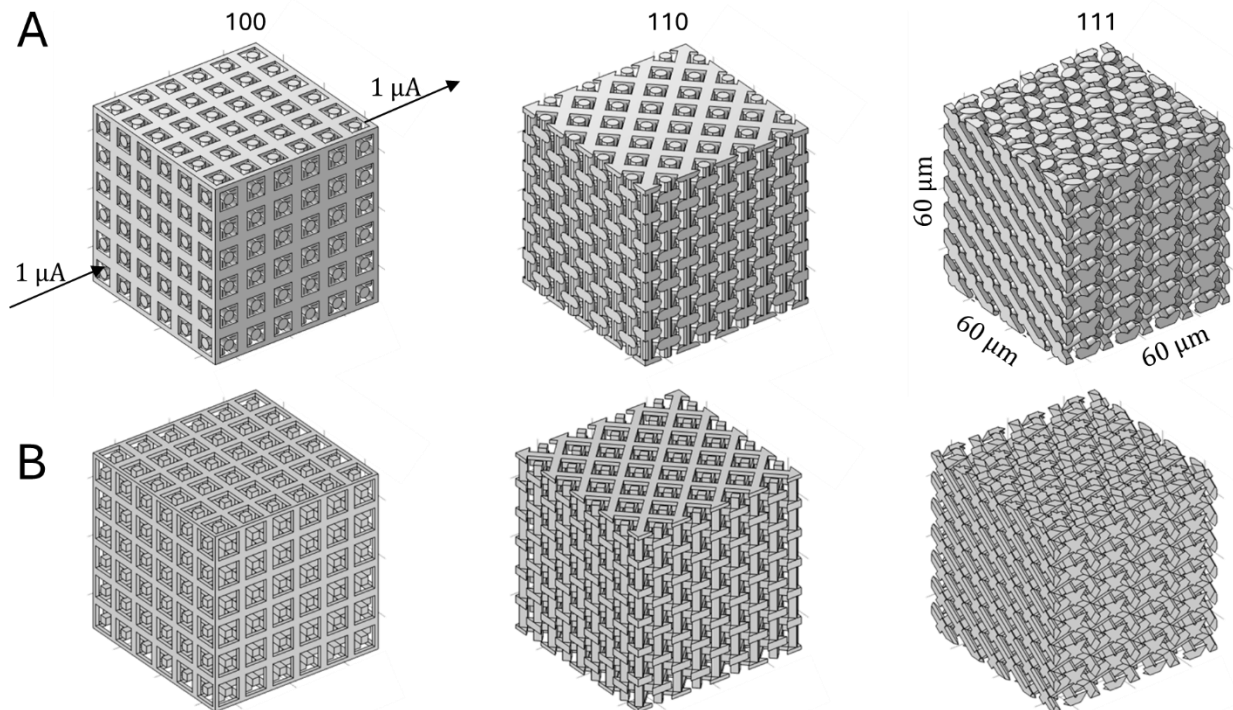


**Figure A3** Cells modeled as body-centered cubic lattices of 3D-crosses of circular (**A**) and square (**B**) cross-section, with cell volume fractions of 48.5% and 31.3%, respectively.

## Results

### Field distributions

As expected, the potential distribution was linear from one electrode to the other, whereas the E-field was very high in the extracellular space and extremely low inside the cells due to the highly resistive membrane (Fig. A4, showing representative examples for 2D and 3D models).

### Effective conductivity

The effective conductivity calculated from the total resistance of the tissue blocks for a given cell volume fraction were averaged across different orientations of the tissue structure relative to the main direction of the E-field (Fig. A5). The coefficient of variation (ratio of the standard deviation to the mean) for each combination of tissue type and cell volume fraction was less than 0.03, showing that the orientation of the tissue structure had no impact on the effective conductivity. Further, the conductivity of different cell shapes for the same tissue type agreed very well with each other, indicating that the conductivity was not affected significantly by cell shape either.

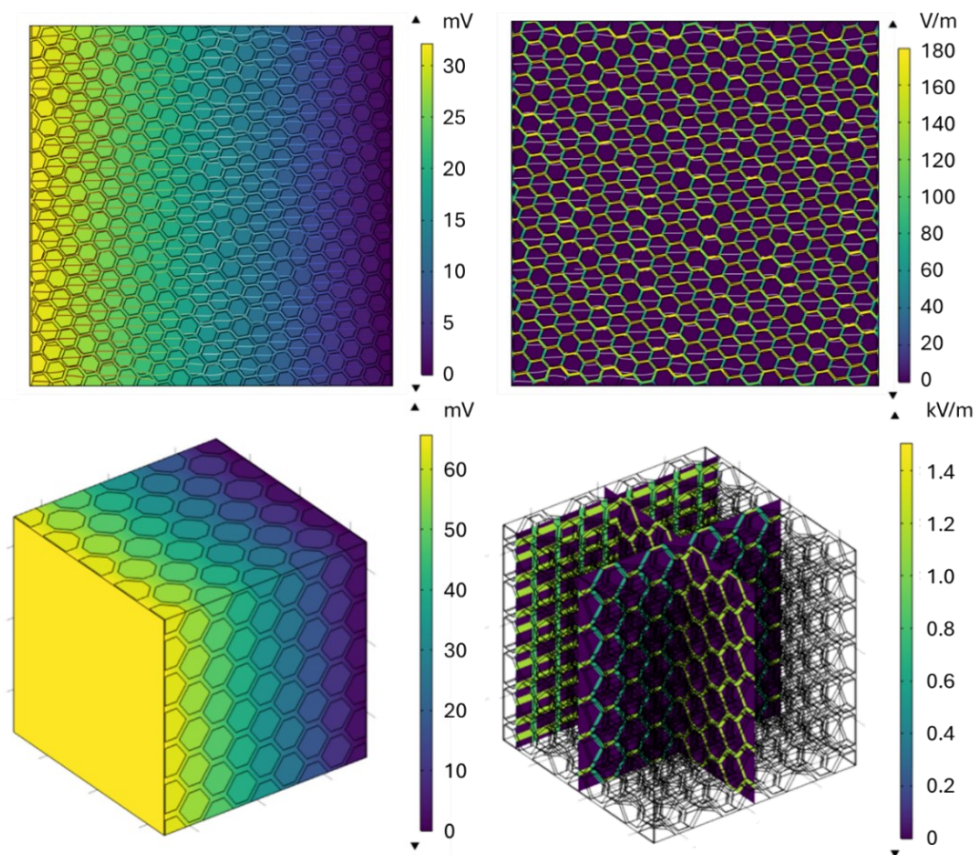


**Figure A4** Example potential (left) and E-field amplitude (right) distributions. Top: 2D model of hexagonal axon grid with 70% cell volume fraction. Bottom: 3D model of truncated octahedron cells with 65% cell volume fraction.

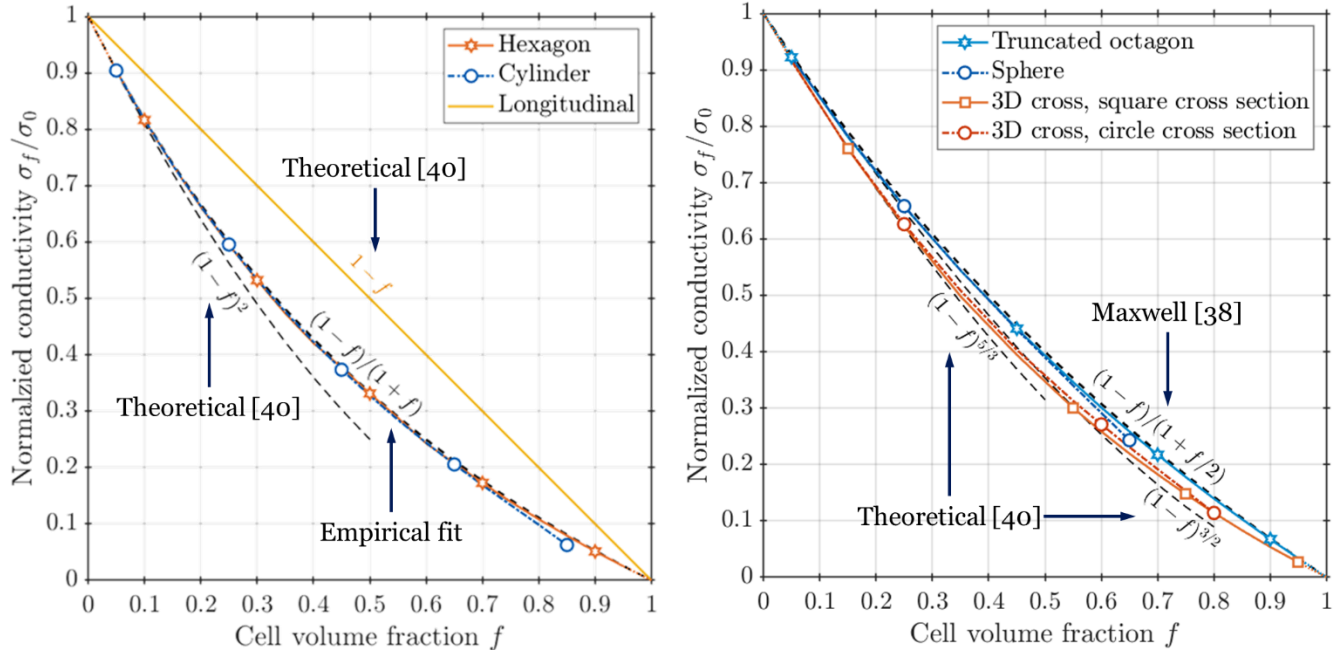


**Figure A5** Effective tissue conductivity normalized to extracellular fluid as function of volume fraction and averaged across orientations. Left: 2D models (average of 7 orientations). Right: 3D models (average of 3 orientations). The conductivity is not affected by the cell shape as demonstrated by the overlapping lines for the same tissue type. Theoretical formulas and empirical fits are also given as dashed lines.

The effective tissue conductivities for the three modeled tissue structures were monotonically decreasing convex functions of the cell volume fraction. They followed the theoretical power formula [40] only for small volume fractions (< 20%) and deviated to higher values for larger volume fractions. The convexity of the relationship amplifies differences in cell volume fraction, resulting in larger conductivity contrasts than assumed from a linear relationship [9]. Surprisingly, Maxwell’s formula, which was originally developed for dilute cell suspension, matched the relationship for the entire range of volume fractions and an empirical relationship inspired by Maxwell’s formula fitted the axonal transverse conductivity (Fig. A5).

*Layer-specific conductivity*

In the cortex and subcortical white matter, around 75% of the cellular volume consists of elongated structures such as axons, dendrites, cilium, and blood vessels (see Table S4 of [23]). Therefore, the conductivity of cortical layers was interpolated using cell volume fractions (Table A1) on simulated results for interleaved neurites (Fig. A6). Here, the conductivity of the extracellular space was assumed to be that of cerebrospinal fluid, 1.8 S/m [46]. The conductivity of subcortical white matter was also estimated for isotropic and anisotropic cases, with the latter using the simulated results for transverse conductivity of parallel axons (Fig. A5, left) and empirical formula for longitudinal conductivity (Table A2).

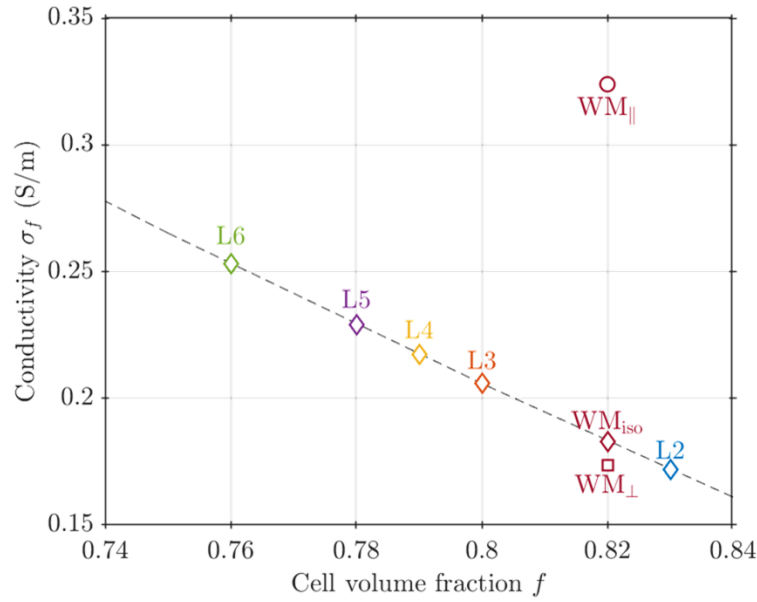


**Figure A6** Effective tissue conductivity of cortical layers shown according to their cell volume fraction, assuming  $\sigma_0$  as 1.8 S/m. Markers are interpolated according to experimental data from [30] (Table S1). The dashed line corresponds to simulated results for interleaved neurites (Fig. A5). White matter conductivity was also calculated for isotropic and anisotropic cases based on its volume fraction.

With decreasing cell volume fraction, the conductivity of cortical layers increased with depth from layer 2 to layer 6 (Fig. A6). Conductivity of layer 1 is estimated to be the lowest (0.14 S/m [16]), in agreement with this trend. Although the variation of conductivity within the cortex was small when compared to the conductivity of the cerebrospinal fluid (9% to 15%), the conductivity difference was considerably larger when compared between layers, e.g., with layers 3 and 6 being 20% and 50% more conductive than layer 2, respectively. This agrees with the higher E-field experimentally measured in layer 2/3 compared to those in layers 4 and 5/6 during tACS [20], in which the large surface electrode resulted in relative uniform current density in the cortex and thus the E-field was inversely proportional to conductivity. With high cell volume fraction, the simulated isotropic white matter conductivity is lower than all layers except layer 2, although it should be noted there is significant difference in the longitudinal and transverse conductivities as expected with anisotropy.

## References

- [1] Peterchev AV, Wagner TA, Miranda PC, Nitsche MA, Paulus W, Lisanby SH, et al. Fundamentals of transcranial electric and magnetic stimulation dose: Definition, selection, and reporting practices. *Brain Stimulat* 2012;5:435–53. <https://doi.org/10.1016/j.brs.2011.10.001>.
- [2] Aberra AS, Wang B, Grill WM, Peterchev AV. Simulation of transcranial magnetic stimulation in head model with morphologically-realistic cortical neurons. *Brain Stimulat* 2020;13:175–89. <https://doi.org/10.1016/j.brs.2019.10.002>.

- [3] Koponen LM, Nieminen JO, Mutanen TP, Stenroos M, Ilmoniemi RJ. Coil optimisation for transcranial magnetic stimulation in realistic head geometry. *Brain Stimulat* 2017;10:795–805. <https://doi.org/10.1016/j.brs.2017.04.001>.
- [4] Wang B, Aberra AS. Bridging macroscopic and microscopic modeling of electric field by brain stimulation 2025:2025.04.07.647453. <https://doi.org/10.1101/2025.04.07.647453>.
- [5] Agudelo-Toro A, Neef A. Computationally efficient simulation of electrical activity at cell membranes interacting with self-generated and externally imposed electric fields. *J Neural Eng* 2013;10:026019. <https://doi.org/10.1088/1741-2560/10/2/026019>.
- [6] Qi Z, Noetscher GM, Miles A, Weise K, Knösche TR, Cadman CR, et al. Enabling electric field model of microscopically realistic brain. *Brain Stimulat* 2025;18:77–93. <https://doi.org/10.1016/j.brs.2024.12.1192>.
- [7] Weise K, Makaroff SN, Numssen O, Bikson M, Knösche TR. Statistical method accounts for microscopic electric field distortions around neurons when simulating activation thresholds. *Brain Stimulat* 2025;18:280–6. <https://doi.org/10.1016/j.brs.2025.02.007>.
- [8] Qi Z, Noetscher GM, Miles A, Weise K, Knösche TR, Cadman CR, et al. Importance of considering microscopic structures in modeling brain stimulation. *Brain Stimulat* 2025;18:1150–2. <https://doi.org/10.1016/j.brs.2025.06.003>.
- [9] Weise K, Makaroff SN, Qi Z, Danskin B, Numssen O, Bikson M, et al. Microscopic electric fields form mesoscale electric fields and influence TMS activation thresholds. *Brain Stimul Basic Transl Clin Res Neuromodulation* 2025;18:1852–4. <https://doi.org/10.1016/j.brs.2025.09.016>.
- [10] Wang B, Hussain MA, Worbs T, Thielscher A, Grill WM, Peterchev AV. Single pointwise samples of electric field on a neuron model cannot predict activation threshold by brain stimulation. *Brain Stimul Basic Transl Clin Res Neuromodulation* 2025;18:1667–70. <https://doi.org/10.1016/j.brs.2025.08.025>.
- [11] Hoeltzell PB, Dykes RW. Conductivity in the somatosensory cortex of the cat — evidence for cortical anisotropy. *Brain Res* 1979;177:61–82. [https://doi.org/10.1016/0006-8993\(79\)90918-1](https://doi.org/10.1016/0006-8993(79)90918-1).
- [12] Goto T, Hatanaka R, Ogawa T, Sumiyoshi A, Riera J, Kawashima R. An Evaluation of the Conductivity Profile in the Somatosensory Barrel Cortex of Wistar Rats. *J Neurophysiol* 2010;104:3388–412. <https://doi.org/10.1152/jn.00122.2010>.
- [13] Karwoski CJ, Frambach DA, Proenza LM. Laminar profile of resistivity in frog retina. *J Neurophysiol* 1985;54:1607–19.
- [14] Wang B, Weiland JD. Resistivity profiles of wild-type, rd1, and rd10 mouse retina. 2015 37th Annu. Int. Conf. IEEE Eng. Med. Biol. Soc. EMBC, Milan, Italy: 2015, p. 1650–3. <https://doi.org/10.1109/EMBC.2015.7318692>.
- [15] Kasi H, Meissner R, Babalian A, van Lintel H, Bertsch A, Renaud P. Direct localised measurement of electrical resistivity profile in rat and embryonic chick retinas using a microprobe. *J Electr Bioimpedance* 2011;1:84–92. <https://doi.org/10.5617/jeb.149>.
- [16] Manola L, Roelofsen BH, Holsheimer J, Marani E, Geelen J. Modelling motor cortex stimulation for chronic pain control: Electrical potential field, activating functions and responses of simple nerve fibre models. *Med Biol Eng Comput* 2005;43:335–43. <https://doi.org/10.1007/BF02345810>.
- [17] Loizos K, RamRakhyani AK, Anderson J, Marc R, Lazzi G. On the computation of a retina resistivity profile for applications in multi-scale modeling of electrical stimulation and absorption. *Phys Med Biol* 2016;61:4491–505. <https://doi.org/10.1088/0031-9155/61/12/4491>.
- [18] Mosayebi-Samani M, Cunha T, Eroğlu HH, Siebner HR, Nitsche MA, Thielscher A. The effect of brain tissue anisotropy on the electric field caused by transcranial electric stimulation: Sensitivity analysis and magnetic resonance electrical impedance tomography. *Imaging Neurosci* 2025;3:imag\_a\_00481. [https://doi.org/10.1162/imag\\_a\\_00481](https://doi.org/10.1162/imag_a_00481).
- [19] Katoch N, Choi B-K, Park J-A, Ko I-O, Kim H-J. Comparison of Five Conductivity Tensor Models and Image Reconstruction Methods Using MRI. *Molecules* 2021;26:5499. <https://doi.org/10.3390/molecules26185499>.
- [20] Lee S, Zhao Z, Alekseichuk I, Park J, Shirinpour S, Linn G, et al. Layers of the monkey visual cortex are selectively modulated during electrical stimulation. *PLOS Biol* 2025;23:e3003278. <https://doi.org/10.1371/journal.pbio.3003278>.
- [21] Wang B, Peterchev AV, Gaugain G, Ilmoniemi RJ, Grill WM, Bikson M, et al. Quasistatic approximation in neuromodulation. *J Neural Eng* 2024;21:041002. <https://doi.org/10.1088/1741-2552/ad625e>.
- [22] Kjer HM, Andersson M, He Y, Pacureanu A, Daducci A, Pizzolato M, et al. Bridging the 3D geometrical organisation of white matter pathways across anatomical length scales and species. *eLife* 2025;13:RP94917. <https://doi.org/10.7554/eLife.94917>.

- [23] Shapson-Coe A, Januszewski M, Berger DR, Pope A, Wu Y, Blakely T, et al. A petavoxel fragment of human cerebral cortex reconstructed at nanoscale resolution. *Science* 2024;384:eadk4858. <https://doi.org/10.1126/science.adk4858>.
- [24] Adler A, Boyle A. Electrical Impedance Tomography: Tissue Properties to Image Measures. *IEEE Trans Biomed Eng* 2017;64:2494–504. <https://doi.org/10.1109/TBME.2017.2728323>.
- [25] Linderholm P, Marescot L, Loke MH, Renaud P. Cell Culture Imaging Using Microimpedance Tomography. *IEEE Trans Biomed Eng* 2008;55:138–46. <https://doi.org/10.1109/TBME.2007.910649>.
- [26] Logothetis NK, Kayser C, Oeltermann A. In Vivo Measurement of Cortical Impedance Spectrum in Monkeys: Implications for Signal Propagation. *Neuron* 2007;55:809–23. <https://doi.org/10.1016/j.neuron.2007.07.027>.
- [27] Pelot NA, Behrend CE, Grill WM. On the parameters used in finite element modeling of compound peripheral nerves. *J Neural Eng* 2019;16:016007. <https://doi.org/10.1088/1741-2552/aaeb0c>.
- [28] Monfared O, Tahayori B, Freestone D, Nešić D, Grayden DB, Meffin H. Determination of the electrical impedance of neural tissue from its microscopic cellular constituents. *J Neural Eng* 2020;17:016037. <https://doi.org/10.1088/1741-2552/ab560a>.
- [29] Wang B, Grill WM, Peterchev AV. Cell Volume Fraction Determines Layer-specific Tissue Conductivity in the Cortex. *Neural Interfaces 2025*, Arlington, VA, USA: 2025.
- [30] Lehmenkühler A, Syková E, Svoboda J, Zilles K, Nicholson C. Extracellular space parameters in the rat neocortex and subcortical white matter during postnatal development determined by diffusion analysis. *Neuroscience* 1993;55:339–51. [https://doi.org/10.1016/0306-4522\(93\)90503-8](https://doi.org/10.1016/0306-4522(93)90503-8).
- [31] Turner NL, Macrina T, Bae JA, Yang R, Wilson AM, Schneider-Mizell C, et al. Reconstruction of neocortex: Organelles, compartments, cells, circuits, and activity. *Cell* 2022;185:1082–1100.e24. <https://doi.org/10.1016/j.cell.2022.01.023>.
- [32] Korogod N, Petersen CC, Knott GW. Ultrastructural analysis of adult mouse neocortex comparing aldehyde perfusion with cryo fixation. *eLife* 2015;4:e05793. <https://doi.org/10.7554/eLife.05793>.
- [33] Tamada H, Blanc J, Korogod N, Petersen CC, Knott GW. Ultrastructural comparison of dendritic spine morphology preserved with cryo and chemical fixation. *eLife* 2020;9:e56384. <https://doi.org/10.7554/eLife.56384>.
- [34] Griswold JM, Bonilla-Quintana M, Pepper R, Lee CT, Raychaudhuri S, Ma S, et al. Membrane mechanics dictate axonal pearls-on-a-string morphology and function. *Nat Neurosci* 2024;1–13. <https://doi.org/10.1038/s41593-024-01813-1>.
- [35] Nicholson C, Hrabětová S. Brain Extracellular Space: The Final Frontier of Neuroscience. *Biophys J* 2017;113:2133–42. <https://doi.org/10.1016/j.bpj.2017.06.052>.
- [36] Velicky P, Miguel E, Michalska JM, Lyudchik J, Wei D, Lin Z, et al. Dense 4D nanoscale reconstruction of living brain tissue. *Nat Methods* 2023;20:1256–65. <https://doi.org/10.1038/s41592-023-01936-6>.
- [37] Nicholson PW. Specific impedance of cerebral white matter. *Exp Neurol* 1965;13:386–401. [https://doi.org/10.1016/0014-4886\(65\)90126-3](https://doi.org/10.1016/0014-4886(65)90126-3).
- [38] Maxwell JC. A treatise on electricity and magnetism. vol. 1. Clarendon press; 1873.
- [39] Rayleigh L. On the influence of obstacles arranged in rectangular order upon the properties of a medium. *Lond Edinb Dublin Philos Mag J Sci* 1892;34:481–502. <https://doi.org/10.1080/14786449208620364>.
- [40] Peters MJ, Stinstra G, Hendriks M. Estimation of the Electrical Conductivity of Human Tissue. *Electromagnetics* 2001;21:545–57. <https://doi.org/10.1080/027263401752246199>.
- [41] Pavlin M, Miklavcic D. The Effective Conductivity and the Induced Transmembrane Potential in Dense Cell System Exposed to DC and AC Electric Fields. *IEEE Trans Plasma Sci* 2009;37:99–106. <https://doi.org/10.1109/TPS.2008.2005292>.
- [42] Meredith RE, Tobias CW. Resistance to Potential Flow through a Cubical Array of Spheres. *J Appl Phys* 1960;31:1270–3. <https://doi.org/10.1063/1.1735816>.
- [43] Roth BJ, Gielen FLH, Wikswow JP. Spatial and temporal frequency-dependent conductivities in volume-conduction calculations for skeletal muscle. *Math Biosci* 1988;88:159–89. [https://doi.org/10.1016/0025-5564\(88\)90041-7](https://doi.org/10.1016/0025-5564(88)90041-7).
- [44] Meffin H, Tahayori B, Sergeev EN, Mareels IMY, Grayden DB, Burkitt AN. Modelling extracellular electrical stimulation: III. Derivation and interpretation of neural tissue equations. *J Neural Eng* 2014;11:065004. <https://doi.org/10.1088/1741-2560/11/6/065004>.
- [45] Tao L, Nicholson C. Maximum geometrical hindrance to diffusion in brain extracellular space surrounding uniformly spaced convex cells. *J Theor Biol* 2004;229:59–68. <https://doi.org/10.1016/j.jtbi.2004.03.003>.
- [46] Baumann SB, Wozny DR, Kelly SK, Meno FM. The electrical conductivity of human cerebrospinal fluid at body temperature. *IEEE Trans Biomed Eng* 1997;44:220–3. <https://doi.org/10.1109/10.554770>.